

Unsupervised Anomaly Detection of Diseases in the Female Pelvis for Real-Time MR Imaging

A. Knupfer^{1,2,*}, J. P. Müller³, J. A. Verdera¹, M. Fenske¹, C. S. Mathy¹, S. Tripathy¹, S. Arndt^{1,4}, M. May¹, M. Uder¹, M. W. Beckmann⁵, S. Burghaus⁵, and J. Hutter²

¹Radiological Institute, University Hospital Erlangen (UKER), Erlangen, Germany

²Institute of Information Processing, Leibniz University Hannover, Hannover, Germany

³Image Data Exploration and Analysis Lab, Friedrich-Alexander University Erlangen–Nürnberg (FAU), Erlangen, Germany

⁴Medical Center for Information and Communication Technology, UKER

⁵Institute of Women’s Health, UKER

*Corresponding author: anika.knupfer@fau.de

Abstract

Pelvic diseases in women of reproductive age represent a major global health burden, with diagnosis frequently delayed due to high anatomical variability, complicating MRI interpretation. Existing AI approaches are largely disease-specific and lack real-time compatibility, limiting generalizability and clinical integration. To address these challenges, we establish a benchmark framework for disease- and parameter-agnostic, real-time-compatible framework for unsupervised anomaly detection in pelvic MRI. The method designs a residual variational autoencoder trained exclusively on healthy sagittal T2-weighted scans acquired across diverse imaging protocols to model normal pelvic anatomy. During inference, reconstruction error heatmaps highlight deviations from learned healthy structure, enabling detection of pathological regions without labeled abnormal data. The model is trained on 294 healthy scans and augmented with diffusion-generated synthetic data to improve robustness. Quantitative evaluation on the publicly available Uterine Myoma MRI Dataset (UMD) yields an average area under the curve (AUC) value of 0.736, with 0.828 sensitivity and 0.692 specificity. Additional inter-observer clinical evaluation extends analysis to endometrial cancer, endometriosis, and adenomyosis, revealing the influence of anatomical heterogeneity and inter-observer variability on performance interpretation. With a reconstruction time of ≈ 92.6 frames per second, the proposed framework establishes a baseline for unsupervised anomaly detection in the female pelvis and towards future integration into real-time MRI. Code is available upon request (<https://github.com/AniKnu/UADPelvis>), prospective data sets are available for academic collaboration.

1 Introduction

Pelvic diseases pose a significant health challenge for women of reproductive age, affecting approximately 40 % of this population [1] and contributing to 4.5 % of the global disease burden [2]. These conditions include uterine myomas, adenomyosis, endometriosis, ovarian tumors, and endometrial or cervical cancer, among others — each presenting unique diagnostic challenges due to their variable appearance in medical imaging [3]. This variability often results in diagnostic delays, misclassification, unnecessary suffering, and, in some cases, avoidable surgical interventions. For example, endometriosis affects about 10 % of women, yet is often misdiagnosed, with an average delay of eight years and nearly 75 % of patients initially misdiagnosed [4,5]. An important factor contributing to the complexity of pelvic disease diagnosis is the substantial anatomical variability of the uterus. While the anteverted and anteflexed positions are most common in healthy uteri, other orientations, such as retroverted, retroflexed, or intermediate, represent normal variants [3] (see Fig. 1).

Currently, detecting and localizing pelvic diseases is time-consuming and costly. While ultrasound is widely used for detection, its interpretability can vary and acoustic shadowing potentially affecting lesion size estimation or risking misinterpretations [6]. In contrast, MRI plays a critical role in more complex

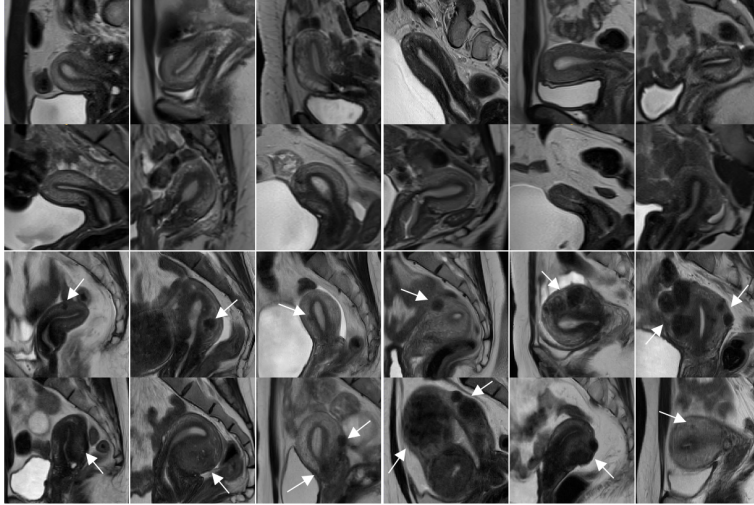


Figure 1: The upper rows depict healthy uteri, while the lower rows represent pathological cases, with arrows indicating anomalies such as myomas, cysts, and endometriosis, highlighting the anatomical variability of the female pelvis.

cases due to its superior spatial resolution, better visualization of deep pelvic structures, improved soft tissue contrast and characterization, broader field of view, and reduced operator dependence, ultimately enabling more accurate diagnosis and treatment planning [7, 8]. However, the lack of standardized protocols and often oblique position of the uterus resulting in unusual planes for pelvic MRIs complicates matters further, as diagnoses depend on the clinician’s expertise and on the images acquired at the time of the scan [9]. A real-time MRI scan that can quickly detect and localize pelvic diseases could significantly improve diagnostic speed and accuracy, reduce risks, and improve patient outcomes.

The integration of Artificial Intelligence (AI) into relatively invariant areas such as brain or chest imaging offers the potential to address these challenges by assisting radiologists in identifying potential anomalies, improving diagnostic accuracy, and supporting clinical decision-making [10]. However, these methods often fail when applied to anatomically variable regions like the abdomen and pelvis, where high inter-patient variability poses unique challenges for generalization, emphasizing the need for specialized approaches tailored to these complex areas [11]. This integration could, in the case of female reproductive health, improve treatment outcomes, and a more personalized approach [12, 13]. However, the considerable variability of both normal and abnormal tissues in the female pelvis described above also presents a significant challenge for current machine learning models [14]. Given the wide range of pelvic disease manifestations, it is not feasible to capture all possible abnormalities in a data set for supervised learning, which has been contributed to date in isolated AI research with specific disease foci [13]. Furthermore, inter-observer variability in the interpretation of pelvic MRI images can lead to significant differences in expert annotations, reflecting clinical reality and complicating the creation of consistent reference standards for supervised deep learning [15]. To address these limitations, unsupervised anomaly detection (UAD) has emerged as a promising approach in medical imaging. UAD allows AI models to learn the distribution of normal data, essentially, healthy anatomy, without the need to label abnormal data. This approach mirrors human learning, wherein anomalies are recognized by first understanding what is “normal” and then identifying deviations. Training deep learning models with healthy data enables the resulting models to detect anomalies by highlighting areas where the model’s reconstruction deviates from the inputs [16–21].

Contributions. This study presents a baseline for disease-independent deep learning models for UAD in the female pelvis. To account for the considerable diversity of acquisition parameters, the model is not subject to protocol restrictions but is trained on a variety of T2-weighted (T2w) sagittal pelvic examinations acquired across field strengths. Beyond quantitative performance evaluation, this work demonstrates how anatomical diversity and expert interpretation influence anomaly detection results, providing important context for evaluating UAD methods in pelvic MRI. The demonstrated low latency inference approach paves the way for future integration into real-time MRI workflows.

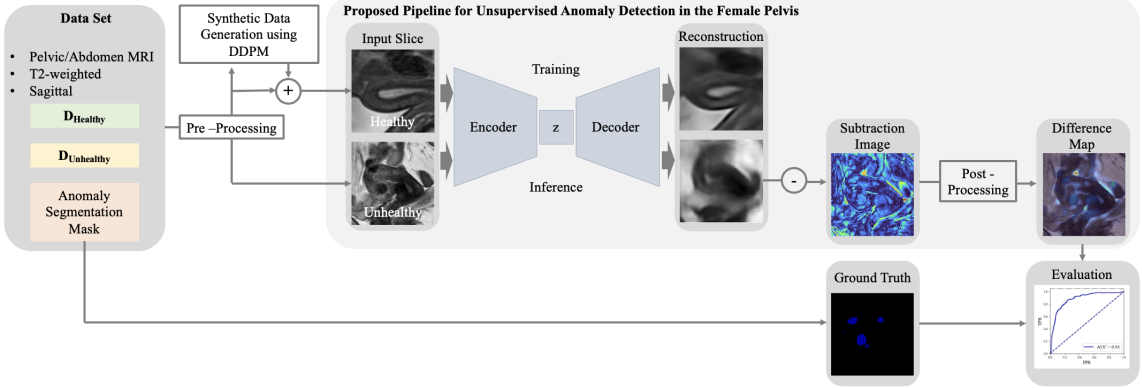


Figure 2: Overview of the proposed unsupervised pelvic MRI anomaly detection pipeline. Preprocessed sagittal T2w scans are augmented using an in-house DDPM and used to train a residual variational autoencoder on healthy anatomy. During inference, reconstruction errors are post-processed and overlaid to highlight anomalies. Evaluation is based on ground-truth segmentations.

2 Related Work

Recent studies have applied deep learning to anomaly detection in the female pelvis across imaging modalities. In ultrasound, Yang et al. [22] proposed a real-time supervised approach for uterine myoma detection, while Huo et al. [23] introduced a two-stage Convolutional Neural Network (CNN) to support less experienced technicians. Shahzad et al. [24] developed a dual-path CNN for myoma classification, and Chen et al. [25] used CNNs to assess myometrial invasion in endometrial cancer. In MRI, Hodneland et al. [26] segmented endometrial tumors using a CNN, extracting texture features for radiomic profiling, though with reduced performance on non-endometrioid tumors. In [27], Figueiredo et al. proposed a five-step deep learning pipeline for detecting rectosigmoid endometriosis in T2w MRI, achieving 96.67 % patient classification and a Dice score of 65.44 %. However, both mentioned MRI studies were limited by small data sets and dependency on specific imaging protocols and disease characteristics.

UAD specifically has emerged as a promising alternative in areas such as in brain MRI where Baur et al. [17] demonstrated that convolutional autoencoders can outperform conventional methods in lesion detection. Raad et al. [18] achieved 83 % accuracy in detecting neonatal encephalopathy using an unsupervised deep autoencoder. While these approaches highlight the potential of UAD, their application to pelvic imaging remains largely unexplored.

Generative models, including variational autoencoders (VAE), generative adversarial networks (GAN), and diffusion models, have already been extensively investigated for UAD. Previous work has demonstrated their potential for various organs, including GAN-based approaches for prostate MRI [21], autoencoder benchmarks for detecting multiple sclerosis lesions highlighting the advantages of VAEs [16], and diffusion-based reconstruction of local brain anatomy [20]. While image-conditioned diffusion models can generate realistic pseudo-healthy reconstructions [28], self-supervised anomaly generation methods face an inherent tradeoff between realism and detectability due to challenges in plausibly integrating synthetic lesions [19]. Self-supervised approaches often rely on synthetic anomaly generation through cut-and-paste strategies or structured noise, but face an inherent tradeoff between realism and detectability of the generated lesions [19, 29]. Despite these advances, UAD remains largely unexplored in female pelvic MRI, where high anatomical variability and non-standardized acquisition protocols pose substantial challenges for robust and generalizable model development.

3 Materials and Methods

The following methodology establishes a baseline approach for UAD in pelvic MRI, prioritizing generalizability across acquisition protocols and disease types. The full UAD pipeline is depicted in Fig. 2, encompassing pre-processing, synthetic data generation, training of the variational autoencoder (VAE), post-processing, and performance evaluation.

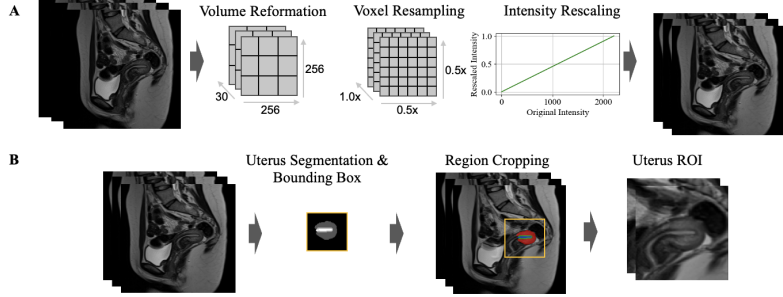


Figure 3: Pre-processing pipeline for standardized model input, including voxel and intensity normalization, anatomical segmentation using an attention-based 3D U-Net [33], and segmentation-driven bounding cropping.

3.1 Data Sets

To construct the training data set $D_{Healthy}$, a PACS query was performed to identify pelvic MRI examinations acquired in female patients from the local university hospital that included a sagittal T2-weighted view of the uterus, as this is the most commonly acquired contrast and orientation. This query spanned a wide range of clinical indications, including but not limited to suspected endometriosis, uterine cancer, rectal pathology, and hip evaluation. A total of 800 recent examinations fulfilling these criteria were identified, retrospectively reviewed by an experienced radiologist and categorized into four groups: no uterus, healthy uterus, minor anomalies, and major anomalies. Only cases with normal uterine anatomy were included, resulting in 294 healthy T2-weighted scans. All data were fully anonymized in line with the institutional ethics guidelines (ethics number: 24-304-Br). The data set exhibits substantial acquisition and physiological variability due to the absence of standardized pelvic MRI protocols. Variations include field strengths (0.55 – 3 T), sequence types (TSE, HASTE), matrix sizes (208 × 208 – 832 × 832), scanner vendors (Siemens, Philips), contrast agent usage, menstrual cycle phase, bladder filling, and patient age (mean 30.01 years). This diversity improves the generalizability of the model and supports realistic synthetic data generation.

The evaluation data set $D_{Unhealthy}$ comprises 242 pathological sagittal T2w pelvic MRI scans from two sources. The public Uterine Myoma MRI Dataset (UMD) [30, 31] provides standardized acquisitions obtained on Philips scanners with fixed protocols and motion-reduction techniques, enabling reproducible quantitative evaluation. UMD annotations were generated by 11 experts using ITK-SNAP [32], labeling uterine structures, myomas, and Nabothian cysts according to FIGO classification. Additionally, 33 in-house pathological cases were selected based on validated radiological reports and ICD codes, including uterine myomas, endometrial cancer, endometriosis, and adenomyosis. Lesion ground truth (GT) segmentations were independently generated by two experienced radiologists and one unexperienced observer to assess annotation-related variability. $D_{Unhealthy}$ includes patients with a mean age of 48.80 years. The two subsets are referred to as $D_{Unhealthy(UMD)}$ and $D_{Unhealthy(in-house)}$, and collectively as $D_{Unhealthy}$.

3.2 Pre-Processing

MRI volumes from both $D_{Healthy}$ and $D_{Unhealthy}$ were converted from DICOM format [34] to NIfTI [35] using SimpleITK [36]. Volumes were resampled to a uniform voxel spacing of $0.5 \text{ mm} \times 0.5 \text{ mm} \times 1 \text{ mm}$, resized to $256 \times 256 \times 30$ voxels, and intensity-normalized to $[0, 1]$, ensuring spatial and numerical consistency. To focus on the uterine region, volumes were cropped using segmentation-guided bounding boxes (Fig. 3). An in-house, deeply supervised attention-based 3D U-Net [33], trained on 80 healthy uterine MRI volumes across multiple field strengths (0.55 – 3 T), segmented the endometrium, junctional zone (JZ), and myometrium in $D_{Healthy}$ and $D_{Unhealthy(in-house)}$. Largest connected component filtering removed spurious regions, and segmentations were manually refined with ITK-SNAP [32]. For the UMD data set, provided uterus masks were used directly, with only voxel resampling applied. Bounding boxes of size $96 \times 96 \times n$ (with n denoting slices containing uterine tissue) were generated, enclosing the uterus. MRI volumes, segmentation masks, and anomaly annotations were cropped accordingly and used as input for anomaly detection and data generation. Following exclusion of 91 UMD cases due to incomplete uterine coverage, $D_{Unhealthy}$ comprised 242 volumes (2,966 UMD, 401 in-house slices) and $D_{Healthy}$ comprised 294 volumes (2,820 slices).

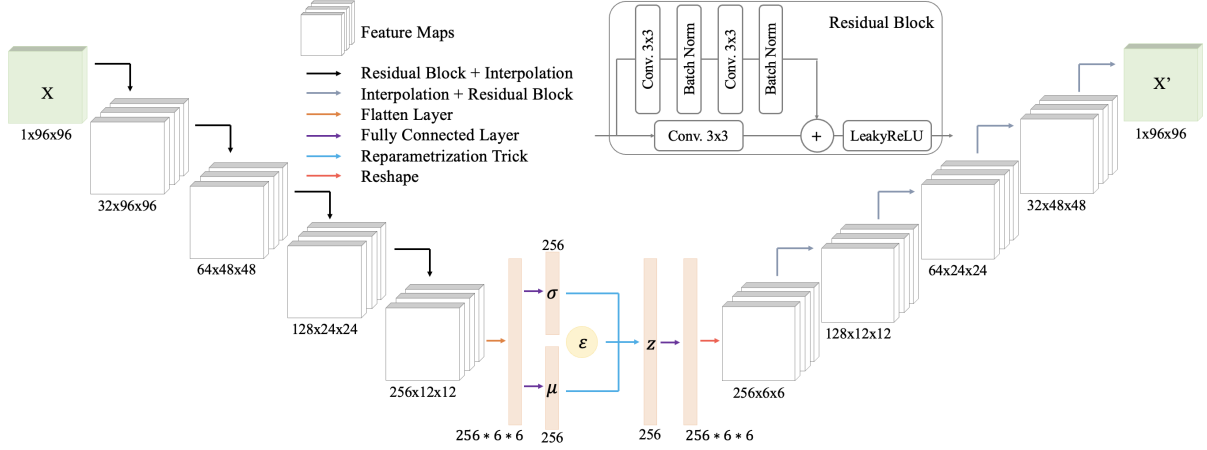


Figure 4: Residual variational autoencoder architecture with four residual blocks in each encoder and decoder, with a latent space dimension of 256.

3.3 Diffusion Model for Synthetic Image Generation

To address data scarcity and variability in healthy female anatomy, a DDPM is employed to generate synthetic T2w pelvic MR images [37]. The model architecture is based on the Hugging Face UNet2DModel following the U-Net design proposed by Ronneberger et al. [38, 39] and integrated into a DDPM framework. Healthy 3D volumes are decomposed into 2D slices, normalized, and used to train an unconditioned diffusion model according to established implementations [40]. Synthetic images are generated from a pre-trained checkpoint using varying random seeds for diversity.

To mitigate risks of model memorization, Structural Similarity Index (SSIM) is employed to quantify the perceptual similarity between real and synthetic image pairs. Synthetic images are compared to their nearest real counterpart, and samples with $\text{SSIM} > 0.35$ are excluded. This empirically chosen threshold ensures sufficient visual dissimilarity while preserving anatomical realism. Applying this criterion resulted in a final set of 1,400 synthetic pelvic MRI slices. Qualitative evaluation is conducted by inspecting randomly sampled synthetic images to assess anatomical plausibility, variability in uterine orientation, contrast characteristics, and the presence of realistic acquisition artifacts. The retained synthetic images are combined with the original healthy data to form the expanded training set $D_{\text{Healthy_Gen}}$.

3.4 Unsupervised Anomaly Detection Pipeline

3.4.1 Data Loader

To prevent data leakage, scans from the same patient were not split across training and validation. An 80:20 train/validation split was applied to D_{Healthy} , ensuring anatomical variability in the validation data, while synthetic samples were used exclusively for training. No data from D_{Healthy} is used for inference to preserve the integrity of the limited training data. Volumes were sliced along the z -axis into 96×96 grayscale 2D images. Each training slice was augmented up to three times using horizontal flips ($p = 0.9$), vertical flips ($p = 0.7$), and Contrast Limited Adaptive Histogram Equalization (CLAHE, $p = 0.7$, clip limit 0.03) [41]. All slices were shuffled and a batch size of 32 was used to account for the heterogeneity of the data set.

3.4.2 Model Architecture and Training

The proposed model is a Residual Variational Autoencoder (ResVAE), illustrated in Fig. 4, which integrates residual blocks within a VAE framework to improve anatomical feature preservation. The encoder and decoder each comprise four residual blocks with channel dimensions of 32, 64, 128, and 256 (mirrored in the decoder). Each block consists of convolutional layers with batch normalization, residual connections, and Leaky ReLU activation. The encoder maps each 2D MRI slice to a 256-dimensional latent space, parameterized by $\mu(x)$ and $\sigma(x)$, with latent sampling performed via reparameterization. This dimensionality balances representational capacity for complex pelvic anatomy with regularization to discourage memorization of pathological patterns. The decoder reconstructs the input using bilinear upsampling with a scale factor of 2.

Training is performed for 100 epochs using the AdamW optimizer (learning rate 1×10^{-4}), with early stopping (patience 15) and gradient clipping (maximum norm 1.0). The loss function combines pixel-level, structural, latent-space, and perceptual constraints, including MSE, SSIM, KL divergence with annealed β (increased from 1×10^{-5} to 1×10^{-4} over the first 100 epochs), and a perceptual loss computed using a ResNet-50 pretrained on RadImageNet [42]. Perceptual features are extracted from the first two residual stages of the network, weighted by 0.3 and 0.15, respectively. The overall training objective is defined as:

$$\begin{aligned} \text{Total Loss}_{\text{UAD}} = & \text{MSE Loss} + 0.5 \times \text{SSIM Loss} \\ & + \beta(\text{epoch}) \times \text{KL Divergence} \\ & + 0.3 \times \text{Perceptual Loss}_{\text{RadImageNet}} \end{aligned} \quad (1)$$

3.4.3 Post-Processing

During inference, scans from $D_{\text{Unhealthy}}$ are processed by the trained ResVAE to generate reconstructions. A residual image is computed as the difference between input and reconstruction, highlighting regions of abnormal deviation. To improve interpretability, the residual map is post-processed by applying a threshold at the 20th percentile, selected empirically to maximize AUC, thereby suppressing low-magnitude errors. To emphasize anatomically relevant regions, a smooth radial weighting mask centered on the uterus is applied, defined by a Gaussian-like function of the Euclidean distance from the image center:

$$d(\text{center}_x, \text{center}_y) = \sqrt{(x - \text{center}_x)^2 + (y - \text{center}_y)^2} \quad (2)$$

$$\text{Mask} = \exp\left(-\frac{d(\text{center}_x, \text{center}_y)^2}{2 \times r^2}\right) \quad (3)$$

where r is set to 30 pixels, as determined through empirical evaluation. Finally, the residual map is squared and smoothed using a median filter (kernel size 5) to reduce noise and enhance regions of high reconstruction error.

3.4.4 UAD Performance Analysis

The anomaly detection pipeline is evaluated under two complementary settings. First, quantitative benchmarking is performed on $D_{\text{Unhealthy}(UMD)}$ to provide a standardized performance assessment, including an ablation study on the impact of synthetic data augmentation by comparing models trained with and without synthetic samples under identical conditions. The evaluation uses GT segmentations and standard metrics (Accuracy, Precision, Sensitivity, Specificity), with localization assessed via reconstruction error maps. ROC curves are computed and AUC is reported as a threshold-independent measure. Second, the model is applied to $D_{\text{Unhealthy}(in-house)}$ to assess the impact of inter-observer variability by comparing identical predictions against annotations from multiple observers. This further enables evaluation across additional pathologies, including endometrial cancer, endometriosis, and adenomyosis.

4 Results

The evaluation of the proposed UAD framework includes an ablation study to quantify the effects of synthetic data augmentation and an analysis of interobserver variability. In addition, the generated synthetic images are evaluated qualitatively.

4.1 Data Set

The data sets exhibit substantial anatomical and technical imbalances. Uterine positioning is heavily skewed toward anteflexed (AF) configurations across all data sets: 88.09% in the training set (182 anteverted (AV), 77 retroverted (RV)), 68.26% in $D_{\text{Unhealthy}(UMD)}$ (74 AV, 68 RV), and 84.85% in the in-house subset. Retroflexed (RF) cases are markedly underrepresented, with only 35 scans in training data (14 AV, 21 RV), 66 in $D_{\text{Unhealthy}(UMD)}$ (46 AV, 20 RV), and 5 in the in-house subset (3 AV, 2 RV). Field-strength distributions are similarly imbalanced. While D_{Healthy} comprises 56.46% high-field 3.0 T scans (alongside 60 at 1.5 T and 68 at 0.55 T), $D_{\text{Unhealthy}(UMD)}$ was acquired exclusively at 3.0 T. The

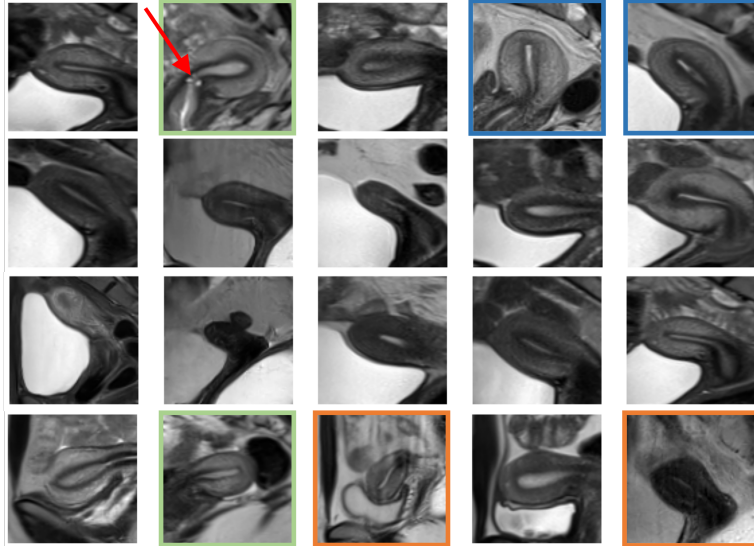


Figure 5: Random synthetic samples illustrating uterine orientations (blue: RV, AF, green: RV, RF), image artifacts (orange), and Nabothian cysts (red arrows).

Table 1: Performance metrics and AUC for pathology detection on $D_{Unhealthy(UMD)}$ for models trained with and without synthetically generated data. Thresholds come from ROC curves. Best overall per-metric values are highlighted in bold.

Training data	Accuracy↑		Precision↑		Sensitivity↑		Specificity↑		AUC↑	
	w/	w/o								
Uterine Myoma	0.618	0.625	0.067	0.068	0.740	0.708	0.619	0.629	0.646	0.627
Nabothian Cyst	0.765	0.732	0.035	0.021	0.936	0.895	0.765	0.732	0.826	0.791
Overall average	0.692	0.679	0.051	0.045	0.838	0.802	0.692	0.681	0.736	0.709

in-house subset exhibits a different pattern with predominantly lower field strengths (2, 21, and 10 scans at 3.0 T, 1.5 T, and 0.55 T, respectively).

4.2 Synthetic Data Generation

Random samples from $D_{Healthy_Gen}$ demonstrate substantial variability in the generated data. As depicted in Fig. 5, the AV, AF uteri position is most frequently synthesized, while RV, AF (blue borders) and RV, RF (green borders) uteri are also represented. The absence of AV, RF position reflects the corresponding imbalance in the real training data (Sec. 4.1). The generated images further capture both anatomical and acquisition-related variability. Orange borders indicate simulated artifacts, and the red arrow denotes the presence of Nabothian cysts. The samples exhibit diverse contrast profiles, including low uterine–background contrast and markedly higher contrast with reduced uterine signal intensity. Variations in myometrial signal intensity are also observed, as well as differences in uterine size, with one example (last row, second from right) demonstrating a markedly enlarged uterus, highlighting the diversity represented by the synthetic data.

4.3 Unsupervised Anomaly Detection Performance

4.3.1 Ablation Study

Results on $D_{Unhealthy(UMD)}$ (Tab. 1) demonstrate that synthetic data augmentation consistently improves model performance across multiple pathologies. The largest gains are observed for Nabothian cysts, with accuracy increasing from 0.732 to 0.765 and AUC from 0.791 to 0.826. For uterine myomas, synthetic augmentation mainly enhances sensitivity from 0.708 to 0.740 and improves the AUC from 0.627 to 0.646.

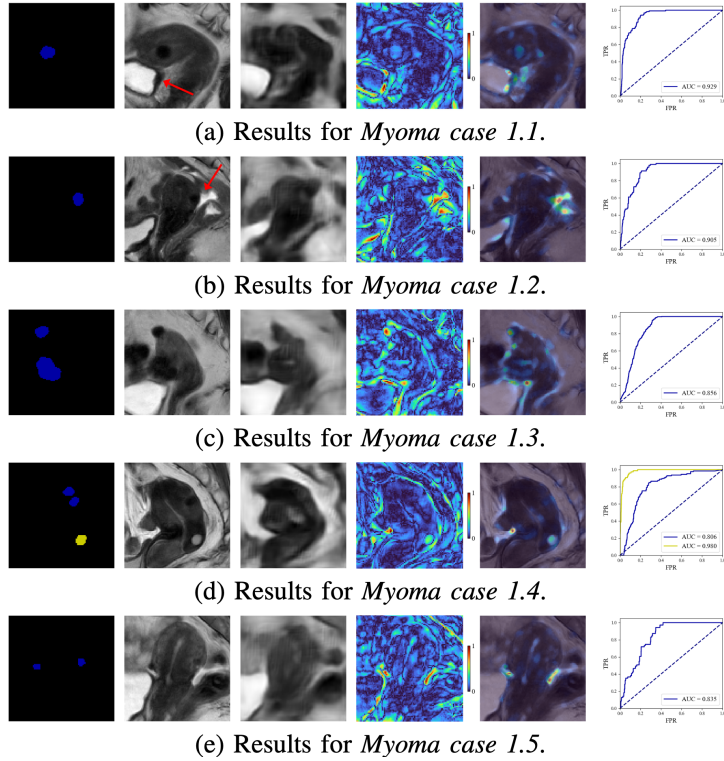


Figure 6: Example cases from $D_{\text{Healthy}}(\text{UMD})$ including uterine myomas (blue) and Nabothian cysts (yellow). Original images, reconstructions, and subtraction maps are displayed as heat maps with an error range of $[0, 1]$. Post-processed difference maps are overlaid on the original images with 50% transparency, and corresponding ROC curves are presented on the right, color-coded by pathology.

4.3.2 Pathologies

The following results demonstrate the pathology-specific performance of the model trained with synthetic data augmentation. As summarized in Tab. 1, Nabothian cyst detection achieves the highest scores for most evaluation metrics. However, despite high sensitivity and AUC, precision remains comparatively low (0.35). In contrast, uterine myomas indicate higher precision (0.67), albeit with lower overall sensitivity and AUC values. Fig. 6 depicts representative cases from the $D_{\text{Healthy}}(\text{UMD})$, including uterine myomas and Nabothian cysts. Each example illustrates the corresponding GT segmentation, the original image, the reconstruction, the subtraction map, and the post-processed error overlay, as well as the associated ROC curve. Cases from the UMD and in-house cohorts are denoted as 1.x and 2.x, respectively.

In several myoma cases (cases 1.1 and 1.2), high AUC values (0.929 and 0.905, respectively) are achieved, while at the same time localized reconstruction errors occur that extend beyond the annotated lesion boundaries, particularly in the area near adjacent pelvic structures, which are highlighted with a red arrow. These areas reflect potential abnormal tissue that is not captured by the segmentations. Case 1.3 indicates reduced performance (AUC 0.856), which is associated with a more anteverted uterine orientation in the reconstruction image, resulting in spatially distributed reconstruction error. In case 1.5, small uterine myomas demonstrate heterogeneous reconstruction errors, with the anterior myoma more clearly detected than the posterior one, which exhibits minimal contrast changes to surrounding tissue. Increased reconstruction error is additionally observed in adjacent brighter tissue posterior to the uterus.

4.3.3 Uterine Positions

The model’s ability to detect pathologies across different uterine positions on $D_{\text{Healthy}}(\text{UMD})$ is depicted in Tab. 2, reporting performance metrics averaged over all segmentations. Performance remains comparable across positions, with AUC values ranging from 0.655 to 0.699. The highest sensitivity (0.811) and AUC (0.699) are observed for the AF, RV position, while the RF, RV cases achieve the highest accuracy (0.665) and specificity (0.686). In contrast, the RF, AV orientation exhibits the lowest accuracy, specificity, and AUC among all.

Table 2: Model performance across uterine positions (AV: anteverted, RV: retroverted, AF: anteflexed, RF: retroflexed) on $D_{Unhealthy(UMD)}$, averaged across all segmentations. Best per-metric values are highlighted in bold.

Position	Accuracy↑	Precision↑	Sensitivity↑	Specificity↑	AUC↑
AF, AV	0.645	0.066	0.757	0.640	0.665
RF, AV	0.624	0.063	0.771	0.626	0.655
AF, RV	0.640	0.060	0.811	0.641	0.699
RF, RV	0.665	0.053	0.694	0.686	0.669

Table 3: Mean lesion volumes (in mL \pm stdv) for each pathology in $D_{Unhealthy(in-house)}$, reported separately for two experienced radiologists and one unexperienced observer (UO), illustrating inter-observer variability. The number of annotated cases is given in brackets.

Lesion type	Radiologist 1	Radiologist 2	UO
Uterine Myoma	78.97 ± 88.19 (16)	69.23 ± 84.03 (14)	73.83 ± 88.56 (11)
Nabothian Cyst	0.55 ± 0.65 (16)	0.46 ± 0.47 (14)	0.45 ± 0.60 (12)
Endometrial Cancer	115.03 ± 126.43 (5)	66.72 ± 74.38 (3)	297.97 ± 240.35 (5)
Endometriosis	21.62 ± 17.46 (3)	7.74 ± 0.00 (1)	36.38 ± 48.37 (3)
Adenomyosis	4.95 ± 7.64 (7)	14.72 ± 7.31 (5)	15.93 ± 12.09 (7)

4.3.4 Run-Time Evaluation

Real-time applicability was assessed by measuring inference reconstruction time of the VAE-based UAD pipeline. Experiments were conducted on an Apple M3 GPU (10-core, Metal Performance Shaders). The model achieved a reconstruction time of 10.8 ms per slice, equivalent to 0.324 s per 30-slice volume (\approx 92.6 FPS).

4.4 Inter-Observer Variability and Model Performance

After benchmarking on UMD, evaluation on the in-house cohort reveals that inter-observer variability profoundly impacts both lesion characterization and model performance assessment. Tab. 3 summarizes mean lesion volumes with corresponding standard deviations and the number of annotated cases for each pathology. Annotation consistency correlates with lesion morphology. Focal lesions exhibit minimal volumetric variation (myomas: 69.23 - 78.97 mL, Nabothian cysts: 0.45 - 0.55 mL), while diffuse pathologies show volume ratios up to 4.5 : 1 (endometrial cancer: 66.72 - 297.97 mL, endometriosis: 7.74 - 36.38 mL). Adenomyosis demonstrates pronounced variability both in lesion extent and case inclusion, with Radiologist 1 reporting markedly lower mean volumes (4.95 mL) than the other annotators (> 14 mL). Beyond volumetric disagreement, annotator disagreement also affected case inclusion and pathology categorization, with some cases labeled healthy by Radiologist 1 but pathological by others, as well as inconsistencies between endometrial and cervical cancer classifications and between myoma and adenomyosis annotations.

Fig. 7 exemplifies these categorical inconsistencies, where Radiologist 2 identified a myoma while the others annotated the same case as adenomyosis. Evaluating a single reconstruction (left panel) against these divergent GT segmentations (right panels) yields AUC values spanning 0.490 (adenomyosis, Radiologist 1) to 0.849 (myoma, Radiologist 2), directly demonstrating how annotation variability translates to substantial performance assessment differences. Notably, the highest reconstruction error localizes to the bladder–uterus interface, a region not included in pathological annotations.

Tab. 4 compares performance metrics between experienced radiologists (mean) and an unexperienced observer, revealing substantial differences in the evaluated model performance. Detection performance correlates strongly with lesion morphology (compare Fig. 8 presenting a selection of one case per pathology). Focal pathologies with sharp contrast boundaries achieve highest performance, with Nabothian cysts (mean AUC 0.868, e.g., 0.937 in Fig. 8) and uterine myomas (mean AUC 0.619, e.g., 0.927) exhibiting localized reconstruction errors that align precisely with lesion boundaries. Conversely, diffuse pathologies demonstrate substantially lower detectability due to distributed, interface-aligned errors rather than focal responses. In endometrial cancer (mean AUC 0.515, e.g., 0.649) and adenomyosis (mean AUC 0.664, e.g., 0.700) cases, reconstruction errors are present along anatomical boundaries (endometrial layer, cervix–uterus junction, JZ), while endometriosis achieves intermediate performance (mean AUC 0.683, e.g., 0.839) depending on lesion localization. Cases with minimal signal intensity variation exhibit spatially diffuse reconstruction patterns, demonstrating model sensitivity to global rather than focal deviations. Annotation experience introduces systematic bias, with the unexperienced observer’s anno-

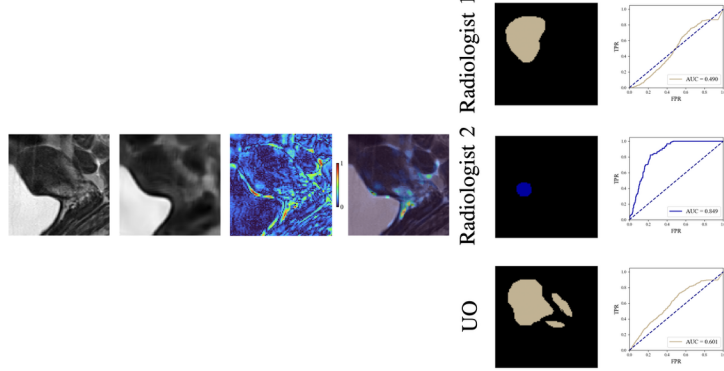


Figure 7: Example from $D_{Unhealthy(in-house)}$ illustrating reconstruction-based anomaly localization with annotations from two expert radiologists and one inexperienced observer (UO). Blue denotes uterine myoma and brown adenomyosis. Corresponding ROC curves are included for each annotator.

Table 4: Performance metrics and AUC for pathology detection in $D_{Unhealthy(in-house)}$, comparing experienced radiologists (mean) and an unexperienced observer. Thresholds are derived from ROC curves. Best and second-best values are highlighted in bold and underlined. Overall performance is reported as a weighted average.

Annotator type	Accuracy↑		Precision↑		Sensitivity↑		Specificity↑		AUC↑	
	Exp	Non								
Uterine Myoma	<u>0.658</u>	0.598	<u>0.098</u>	0.082	0.654	0.717	<u>0.657</u>	0.602	0.619	0.619
Nabothian Cyst	0.800	0.775	0.064	0.025	0.922	0.898	0.798	0.775	0.881	0.868
Endometrial Cancer	0.510	0.495	0.127	0.293	0.677	0.798	0.489	0.414	0.515	0.605
Endometriosis	0.521	<u>0.729</u>	0.056	0.080	<u>0.901</u>	<u>0.837</u>	0.509	<u>0.725</u>	<u>0.683</u>	0.839
Adenomyosis	0.565	0.573	0.082	<u>0.127</u>	0.799	0.781	0.553	0.550	0.664	0.678
Overall Average	0.639	0.627	0.095	0.129	0.762	0.790	0.632	0.612	0.632	0.702

tations yielding higher overall AUC (0.702 versus 0.632) driven primarily by broader lesion delineations that increase true positive rates at the cost of specificity.

5 Discussion

5.1 Summary

This work establishes a foundation for unsupervised anomaly detection in female pelvic MRI. By adopting a disease- and parameter-independent approach that reflects the anatomical complexity and variability of the pelvis, it paves the way for future research and supports the development of AI-driven real-time workflows for pelvic MRI.

5.2 Comparison to the State of the Art

Diagnostic performance of clinical radiological-led interpretation of pelvis MRI, while achieving overall accuracies of 80-90% for benign conditions and above 90% for malignant staging, [43,44], depends strongly on expertise and decreases in atypical or subtle cases [45]. In complex conditions such as deep infiltrating endometriosis, MRI alone is often insufficient [46], contributing to delayed diagnosis and motivating automated real-time decision support.

To date, UAD has not been explored in female pelvic MRI. Prior work in anatomically more homogeneous regions demonstrates, however, the potential of generative models. Baur et al. [16,17,47] reported high AUC values (e.g., 0.945 for multiple sclerosis) using autoencoders and VAE-GANs in brain MRI, while Patsanis et al. [21] applied GAN-based UAD to prostate MRI, achieving moderate performance ($AUC = 0.76$) and reporting sensitivity to anatomical variability. These findings highlight the increasing difficulty of UAD in regions with complex and heterogeneous anatomy as present in the pelvis. Recent large-scale benchmarks, including BMAD [48] and MedAnomaly [49], further demonstrate strong UAD

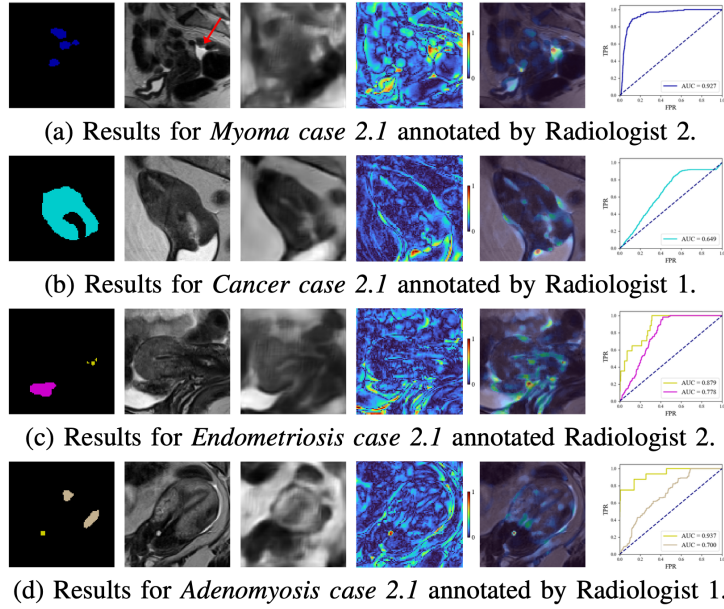


Figure 8: Example cases from $D_{\text{Healthy}}(\text{in-house})$ including uterine myomas (blue), Nabothian cysts (yellow), cancer (cyan), endometriosis (magenta) and adenomyosis (brown). Original images, reconstructions, and subtraction maps are displayed as heat maps with an error range of $[0, 1]$. Post-processed difference maps are overlaid on the original images with 50% transparency, and corresponding ROC curves are presented on the right, color-coded by pathology.

performance across standardized tasks such as brain MRI, liver CT, and chest X-ray. However, these applications support organ-centric cropping, background suppression, or patch-based evaluation, limiting anatomical context. Such assumptions are less applicable to pelvic MRI, where clinically relevant abnormalities often arise from global anatomical alterations, inter-organ relationships, or diffuse tissue changes rather than isolated focal lesions. Consequently, direct benchmarking between these protocols is not methodologically comparable. Within this substantially more challenging setting, our fully unsupervised, disease- and parameter-agnostic approach achieves an overall AUC of 0.736 on the UMD across heterogeneous pelvic pathologies, with strong performance for example for specific findings such as Nabothian cysts ($\text{AUC} = 0.826$). Importantly, these performance values should be interpreted as conservative estimates, as quantitative evaluation is inherently constrained by inter-observer variability and GT definitions limited by a high degree of subjectivity. These findings highlight both the complexity of pelvic anomaly detection and the need to contextualize quantitative metrics within anatomical variability and annotation uncertainty.

5.3 Strengths and Limitations

The proposed UAD pipeline demonstrated several strengths in the detection of female pelvic disease. Notably, it performed comparably across uterine positions, validating the concept of reconstructing healthy anatomy to detect deviations. The model performed particularly well for focal lesions, such as uterine myomas and Nabothian cysts, enabling clear anomaly localization. Another key strength lies in its robustness to imaging variability. Despite the absence of a standardized MRI protocol and substantial heterogeneity in the training data, including variations in field strength, resolution, contrast, and sequence type, the model generalized well to unseen data. This was evidenced by consistent performance across uterine myoma and Nabothian cyst cases in both the UMD and in-house data sets, indicating strong multi-center applicability. Such generalizability is essential for real-world deployment, where diverse acquisition protocols are common. To address limited data availability and increase training diversity, synthetically generated samples expanded the data set, further improving detection robustness, particularly for Nabothian cysts, which already exhibited stable performance prior to augmentation.

A key limitation of the proposed UAD pipeline is its dependence on high-quality and representative training data. Mislabeled or unhealthy cases may cause the model to reconstruct pathological patterns, reducing detection performance. Rare anatomical configurations, such as retroflexed uterine positions, are currently underrepresented, potentially limiting generalization and increasing reconstruction errors.

This imbalance also propagates to synthetic data generation, as DDPMs tend to reproduce dominant anatomical patterns rather than compensate for distribution bias [50]. Architecturally, the probabilistic nature of VAEs introduces output variability, affecting reproducibility and limiting sensitivity to subtle or low-contrast anomalies, including adenomyosis and early-stage malignancies. Moreover, the evaluation of the model is further limited by the quality and consistency of the GT annotations. Inter-observer disagreement arises not only in delineating lesion boundaries, but also in determining whether a case is pathological and in identifying the specific pathology. Especially in the case of adenomyosis, diagnostic discrepancies may stem from reliance on a single sequence, where the condition is often subtle and heavily influenced by the visibility of the JZ [51, 52]. As a result, identical model predictions can yield significantly different performance metrics depending on the reference segmentation. This issue is well documented in medical imaging, where label noise arising from inter-observer variability and inconsistent annotations can significantly impact model performance [15]. In addition, ground-truth masks may omit pathological regions outside the uterine structures, leading to apparent false positives when the model correctly identifies unannotated abnormalities. Together, these findings highlight a fundamental challenge in pelvic MRI: while diagnostic ambiguity motivates the need for real-time decision support, reliable model development and evaluation depend critically on consistent, high-quality reference annotations, emphasizing the importance of standardized labeling, multi-reader consensus, and explicit reporting of inter-observer variability.

5.4 Research and Clinical Implications

The proposed UAD pipeline establishes a disease-agnostic baseline for pelvic anomaly detection on MRI data, enabling identification of diverse pathologies without labeled data with anomalies. Evaluation on the publicly available UMD provides a reproducible benchmark for future studies. Pelvic disease diagnosis is often hindered by anatomical variability, limited awareness of conditions such as endometriosis, and reliance on reader expertise. By highlighting deviations from learned healthy anatomy, the proposed approach offers an objective reference that may support earlier detection and reduce diagnostic delays. Recent work in prostate MRI further demonstrates that AI-based analysis can achieve expert-level or superior diagnostic performance, even without full clinical context [53].

A key clinical application of the proposed UAD framework is its readiness for integration into real-time MRI, analogous to recent advances in fetal imaging, enabling adaptive acquisitions and immediate feedback during scanning [54, 55]. Such integration could optimize imaging protocols, reduce unnecessary interventions, and improve diagnostic efficiency and patient experience. As a disease-agnostic approach, the model may also support radiologist training by highlighting suspicious regions without relying on predefined pathology labels, thereby improving interpretability. Extending the framework to multimodal imaging with additional contrasts such as T1-weighted imaging could further enhance AI-guided pelvic diagnostics and support more equitable reproductive healthcare. In addition, sensitivity to subtle anatomical deviations may offer insights into disease development, particularly for relatively underexplored conditions such as endometriosis [56]. Notably, qualitative review of the unhealthy cohorts revealed regions with consistently high reconstruction error that were not included in the reference annotations (e.g., Fig. 6 a, b), suggesting potential omissions in the ground truth. If such regions correspond to unannotated pathology, quantitative metrics may underestimate true model performance, as the UAD framework is designed to detect any abnormal pelvic tissue rather than only predefined lesion labels.

5.5 Future steps

Expanding the data set to include broader demographic representation and rarer pelvic diseases is essential to improve model robustness and generalizability. Methodologically, integrating alternative architectures and learning paradigms may further enhance UAD performance. Incorporating domain-specific anatomical priors, such as typical uterine shape, size, and spatial configuration, could guide representation learning and improve discrimination between normal and pathological anatomy. In addition, contrastive and self-supervised learning strategies may increase sensitivity to subtle abnormalities by explicitly modeling intra-class anatomical variability without requiring pathological labels. Recent advances in diffusion-based anomaly detection, particularly demonstrated in brain MRI [20, 28], further highlight the potential of these approaches for future application to female pelvic imaging.

6 Conclusion

This work presents a deep generative framework for unsupervised anomaly detection in female pelvic MRI, designed to model the substantial anatomical variability of healthy pelvic anatomy. By learning the distribution of normal tissue, the proposed approach identifies abnormalities as reconstruction deviations, removing the need for annotated pathological data. The low-latency design supports integration into real-time MRI workflows, enabling immediate visual feedback during image acquisition. Such capability has the potential to support radiologists in identifying subtle abnormalities, reduce diagnostic uncertainty, and facilitate more personalized imaging strategies. Overall, this study establishes a benchmark for disease-agnostic anomaly detection in the female pelvis and provides a foundation for future research toward AI-assisted, real-time pelvic MRI.

Acknowledgments

This work was supported by the High Tech Agenda of the Free State of Bavaria, funding from the BayStMGP [EndoKI], DFG Heisenberg funding [502024488] and an ERC Starting grant EARTHWORM [101165242].

References

- [1] Yidan Gao, Xuemei Wang, Qian Wang, Lijuan Jiang, Cuixiu Wu, Yuanshuo Guo, Na Cui, Haoneng Tang, and Lingli Tang. Rising global burden of common gynecological diseases in women of childbearing age from 1990 to 2021: an update from the global burden of disease study 2021. *Reproductive Health*, 22(1), April 2025.
- [2] Joni Sebastian, Cindy Rodriguez, Zachary V. Samuels, Kristen Pepin, and Brian M. Zeglis. Molecular imaging in gynecology: Beyond cancer. *Journal of Nuclear Medicine*, 65(7):998–1003, June 2024.
- [3] S. Sudderuddin, E. Helbren, M. Telesca, R. Williamson, and A. Rockall. Mri appearances of benign uterine disease. *Clinical Radiology*, 69(11):1095–1104, November 2014.
- [4] G. Hudelist, N. Fritzer, A. Thomas, C. Niehues, P. Oppelt, D. Haas, A. Tammaro, and H. Salzer. Diagnostic delay for endometriosis in austria and germany: causes and possible consequences. *Human Reproduction*, 27(12):3412–3416, September 2012.
- [5] Serdar E Bulun, Bahar D Yilmaz, Christia Sison, Kaoru Miyazaki, Lia Bernardi, Shimeng Liu, Amanda Kohlmeier, Ping Yin, Magdy Milad, and JianJun Wei. Endometriosis. *Endocrine Reviews*, 40(4):1048–1079, April 2019.
- [6] Lie Cai and André Pfob. Artificial intelligence in abdominal and pelvic ultrasound imaging: current applications. *Abdominal Radiology*, 50(4):1775–1789, November 2024.
- [7] Asmaa Yousef El said, Nadia Ali Mahmoud, and Hamada Mohamed Khater. Comparative study between mri and ultrasound in evaluation of uterine lesions. *Benha Medical Journal*, 0(0):0–0, February 2025.
- [8] Angela Tong, Adela G. Cope, Timothy L. Waters, Jennifer S. McDonald, and Wendaline M. Van-Buren. Best practices: Ultrasound versus mri in the assessment of pelvic endometriosis. *American Journal of Roentgenology*, 223(6), December 2024.
- [9] Stephanie Nougaret, Yulia Lakhman, Sophie Gourgou, Rahel Kubik-Huch, Lorenzo Derchi, Evis Sala, and Rosemarie Forstner. Mri in female pelvis: an esur/esr survey. *Insights into Imaging*, 13(1), March 2022.
- [10] Vaidehi Satushe, Vibha Vyas, Shilpa Metkar, and Davinder Paul Singh. Ai in mri brain tumor diagnosis: A systematic review of machine learning and deep learning advances (2010–2025). *Chemometrics and Intelligent Laboratory Systems*, 263:105414, August 2025.
- [11] Lie Cai and André Pfob. Artificial intelligence in abdominal and pelvic ultrasound imaging: current applications. *Abdominal Radiology*, 50(4):1775–1789, November 2024.

- [12] Nida Aftab. Artificial intelligence in obstetrics and gynaecology: Advancing precision and personalised care. *Cureus*, June 2025.
- [13] Brie Dungate, Dwayne R Tucker, Emma Goodwin, and Paul J Yong. Assessing the utility of artificial intelligence in endometriosis: Promises and pitfalls. *Women's Health*, 20, January 2024.
- [14] Fatemeh Zabihollahy, Akila N Viswanathan, Ehud J Schmidt, Marc Morcos, and Junghoon Lee. Fully automated multiorgan segmentation of female pelvic magnetic resonance images with coarse-to-fine convolutional neural network. *Medical Physics*, 48(11):7028–7042, October 2021.
- [15] Davood Karimi, Haoran Dou, Simon K. Warfield, and Ali Gholipour. Deep learning with noisy labels: Exploring techniques and remedies in medical image analysis. *Medical Image Analysis*, 65:101759, October 2020.
- [16] Christoph Baur, Stefan Denner, Benedikt Wiestler, Nassir Navab, and Shadi Albarqouni. Autoencoders for unsupervised anomaly segmentation in brain mr images: A comparative study. *Medical Image Analysis*, 69:101952, April 2021.
- [17] Christoph Baur, Benedikt Wiestler, Mark Muehlau, Claus Zimmer, Nassir Navab, and Shadi Albarqouni. Modeling healthy anatomy with artificial intelligence for unsupervised anomaly detection in brain mri. *Radiology: Artificial Intelligence*, 3(3):e190169, May 2021.
- [18] Jad Dino Raad, Ratna Babu Chinnam, Suzan Arslanturk, Sidhartha Tan, Jeong-Won Jeong, and Swati Mody. Unsupervised abnormality detection in neonatal mri brain scans using deep learning. *Scientific Reports*, 13(1), July 2023.
- [19] Matthew Baugh, Jeremy Tan, Johanna P. Müller, Mischa Dombrowski, James Batten, and Bernhard Kainz. Many tasks make light work: Learning to localise medical anomalies from multiple synthetic tasks. In *Medical Image Computing and Computer Assisted Intervention – MICCAI 2023*, page 162–172. Springer Nature Switzerland, 2023.
- [20] Finn Behrendt, Debayan Bhattacharya, Julia Krüger, Roland Opfer, and Alexander Schlafer. Patched diffusion models for unsupervised anomaly detection in brain mri. In *Medical Imaging with Deep Learning*, pages 1019–1032. PMLR, arXiv, 2023.
- [21] Alexandros Patsanis, Mohammed R.S. Sunoqrot, Sverre Langørgen, Hao Wang, Kirsten M. Selnaes, Helena Bertilsson, Tone F. Bathen, and Mattijs Elschot. A comparison of generative adversarial networks for automated prostate cancer detection on t2-weighted mri. *Informatics in Medicine Unlocked*, 39:101234, 2023.
- [22] Tiantian Yang, Linlin Yuan, Ping Li, and Peizhong Liu. Real-time automatic assisted detection of uterine fibroid in ultrasound images using a deep learning detector. *Ultrasound in Medicine & Biology*, 49(7):1616–1626, July 2023.
- [23] Tongtong Huo, Lixin Li, Xiting Chen, Ziyi Wang, Xiaojun Zhang, Songxiang Liu, Jinfa Huang, Jiayao Zhang, Qian Yang, Wei Wu, Yi Xie, Honglin Wang, Zhewei Ye, and Kaixian Deng. Artificial intelligence-aided method to detect uterine fibroids in ultrasound images: a retrospective study. *Scientific Reports*, 13(1), March 2023.
- [24] Ahsan Shahzad, Abid Mushtaq, Abdul Quddoos Sabeeh, Yazeed Yasin Ghadi, Zohaib Mushtaq, Saad Arif, Muhammad Zia ur Rehman, Muhammad Farrukh Qureshi, and Faisal Jamil. Automated uterine fibroids detection in ultrasound images using deep convolutional neural networks. In *Healthcare*, volume 11, page 1493. MDPI AG, May 2023.
- [25] Xiaojun Chen, Yida Wang, Minhua Shen, Bingyi Yang, Qing Zhou, Yiniao Yi, Weifeng Liu, Guofu Zhang, Guang Yang, and He Zhang. Deep learning for the determination of myometrial invasion depth and automatic lesion identification in endometrial cancer mr imaging: a preliminary study in a single institution. *European Radiology*, 30(9):4985–4994, April 2020.
- [26] Erlend Hodneland, Julie A. Dybvik, Kari S. Wagner-Larsen, Veronika Šoltészová, Antonella Z. Munthe-Kaas, Kristine E. Fasmer, Camilla Krakstad, Arvid Lundervold, Alexander S. Lundervold, Oyvind Salvesen, Bradley J. Erickson, and Ingfrid Haldorsen. Automated segmentation of endometrial cancer on mr images using deep learning. *Scientific Reports*, 11(1), January 2021.

- [27] Weslley Kelson Ribeiro Figueiredo, Aristófanes Corrêa Silva, Anselmo Cardoso de Paiva, João Otávio Bandeira Diniz, Alice Brandão, and Marco Aurelio Pinho Oliveira. Automatic segmentation of deep endometriosis in the rectosigmoid using deep learning. *Image and Vision Computing*, 151:105261, November 2024.
- [28] Matthew Baugh, Hadrien Reynaud, Sergio Naval Marimont, Sarah Cechnicka, Johanna P. Müller, Giacomo Tarroni, and Bernhard Kainz. Image-conditioned diffusion models for medical anomaly detection. In *Uncertainty for Safe Utilization of Machine Learning in Medical Imaging*, page 117–127. Springer Nature Switzerland, October 2024.
- [29] Johanna P. Müller, Matthew Baugh, Jeremy Tan, Mischa Dombrowski, and Bernhard Kainz. Confidence-aware and self-supervised image anomaly localisation. In *Uncertainty for Safe Utilization of Machine Learning in Medical Imaging*, page 177–187. Springer Nature Switzerland, 2023.
- [30] Haixia Pan, Minghuang Chen, Wenpei Bai, Bin Li, Xiaoran Zhao, Meng Zhang, Dongdong Zhang, Yanan Li, Hongqiang Wang, Haotian Geng, Weiya Kong, Cong Yin, Linfeng Han, Jiahua Lan, and Tian Zhao. Large-scale uterine myoma mri dataset covering all figo types with pixel-level annotations. *Scientific Data*, 11(1), April 2024.
- [31] Haixia Pan, Minghuang Chen, Wenpei Bai, Bin Li, Xiaoran Zhao, Meng Zhang, Dongdong Zhang, Yanan Li, and Hongqiang Wang. UMD.zip. *figshare*, 6 2023.
- [32] Paul A. Yushkevich, Joseph Piven, Heather Cody Hazlett, Rachel Gimpel Smith, Sean Ho, James C. Gee, and Guido Gerig. User-guided 3d active contour segmentation of anatomical structures: Significantly improved efficiency and reliability. *NeuroImage*, 31(3):1116–1128, July 2006.
- [33] Smiti Tripathy, Nyvenn Castro, Matthias May, Lisa Siegler, Lisa Story, Michael Uder, and Jana Hutter. Deep supervision attention u-net for segmentation of uterine zones: a multi-center study. Presented at the ISMRM & ISMRM Annual Meeting and Exhibition 2025. [Online]. Available: <https://archive.ismrm.org/2025/0105.html>.
- [34] National Electrical Manufacturers Association. Dicom standards, 2021. Accessed: 2025-03-03.
- [35] RW Cox, J Ashburner, H Breman, K Fissell, C Haselgrove, CJ Holmes, JL Lancaster, DE Rex, SM Smith, JB Woodward, and SC Strother. Nifti - neuroimaging informatics technology initiative, 2011. Accessed: 2025-03-03.
- [36] Ziv Yaniv, Bradley C. Lowekamp, Hans J. Johnson, and Richard Beare. Simpleitk image-analysis notebooks: a collaborative environment for education and reproducible research. *Journal of Digital Imaging*, 31(3):290–303, November 2017.
- [37] Jonathan Ho, Ajay Jain, and Pieter Abbeel. Denoising diffusion probabilistic models. *Advances in neural information processing systems*, 2020.
- [38] Olaf Ronneberger, Philipp Fischer, and Thomas Brox. U-net: Convolutional networks for biomedical image segmentation. In *Medical Image Computing and Computer-Assisted Intervention – MICCAI 2015*, page 234–241. Springer International Publishing, 2015.
- [39] Patrick von Platen, Suraj Patil, Anton Lozhkov, Pedro Cuenca, Nathan Lambert, Kashif Rasul, Mishig Davaadorj, Dhruv Nair, Sayak Paul, William Berman, Yiyi Xu, Steven Liu, and Thomas Wolf. Diffusers: State-of-the-art diffusion models, 2022.
- [40] Johanna P. Müller, Anika Knupfer, Pedro Blöss, Edoardo Berardi Vittur, Bernhard Kainz, and Jana Hutter. Diffusing the blind spot: Uterine mri synthesis with diffusion models. *arXiv preprint arXiv:2508.07903*, 2025.
- [41] Ali M. Reza. Realization of the contrast limited adaptive histogram equalization (clahe) for real-time image enhancement. *Journal of VLSI signal processing systems for signal, image and video technology*, 38(1):35–44, August 2004.
- [42] Xueyan Mei, Zelong Liu, Philip M Robson, Brett Marinelli, Mingqian Huang, Amish Doshi, Adam Jacobi, Chendi Cao, Katherine E Link, Thomas Yang, et al. Radimagenet: An open radiologic deep learning research dataset for effective transfer learning. *Radiology: Artificial Intelligence*, 4(5):e210315, 2022.

- [43] Pietro Valerio Foti, Renato Farina, Stefano Palmucci, Ilenia Anna Agata Vizzini, Norma Libertini, Maria Coronella, Saveria Spadola, Rosario Caltabiano, Marco Iraci, Antonio Basile, Pietro Milone, Antonio Cianci, and Giovanni Carlo Ettorre. Endometriosis: clinical features, mr imaging findings and pathologic correlation. *Insights into Imaging*, 9(2):149–172, February 2018.
- [44] Isabelle Thomassin-Naggara, Edouard Poncelet, Aurelie Jalaguier-Coudray, Adalgisa Guerra, Laure S. Fournier, Sanja Stojanovic, Ingrid Millet, Nishat Bharwani, Valerie Juhan, Teresa M. Cunha, Gabriele Masselli, Corinne Balleyguier, Caroline Malhaire, Nicolas F. Perrot, Elizabeth A. Sadowski, Marc Bazot, Patrice Taourel, Raphaël Porcher, Emile Darai, Caroline Reinholt, and Andrea G. Rockall. Ovarian-adnexal reporting data system magnetic resonance imaging (o-rads mri) score for risk stratification of sonographically indeterminate adnexal masses. *JAMA Network Open*, 3(1):e1919896, January 2020.
- [45] Sebastian Harth, Hasan Emin Kaya, Felix Zeppernick, Ivo Meinhold-Heerlein, Jörg Keckstein, Selcuk Murat Yildiz, Emina Nurkan, Gabriele Anja Krombach, and Fritz Christian Roller. Application of the enzian classification for endometriosis on mri: prospective evaluation of inter- and intraobserver agreement. *Frontiers in Medicine*, 10, November 2023.
- [46] E. Pascoal, J. M. Wessels, M. K. Aas-Eng, M. S. Abrao, G. Condous, D. Jurkovic, M. Espada, C. Exacoustos, S. Ferrero, S. Guerriero, G. Hudelist, M. Malzoni, S. Reid, S. Tang, C. Tomassetti, S. S. Singh, T. Van den Bosch, and M. Leonardi. Strengths and limitations of diagnostic tools for endometriosis and relevance in diagnostic test accuracy research. *Ultrasound in Obstetrics & Gynecology*, 60(3):309–327, September 2022.
- [47] Christoph Baur, Benedikt Wiestler, Shadi Albarqouni, and Nassir Navab. Deep autoencoding models for unsupervised anomaly segmentation in brain mr images. In *Brainlesion: Glioma, Multiple Sclerosis, Stroke and Traumatic Brain Injuries*, page 161–169. Springer International Publishing, 2019.
- [48] Jinan Bao, Hanshi Sun, Hanqiu Deng, Yinsheng He, Zhaoxiang Zhang, and Xingyu Li. Bmad: Benchmarks for medical anomaly detection. In *Proceedings of the IEEE/CVF Conference on Computer Vision and Pattern Recognition*, pages 4042–4053, 2024.
- [49] Yu Cai, Weiwen Zhang, Hao Chen, and Kwang-Ting Cheng. Medianomaly: A comparative study of anomaly detection in medical images. *Medical Image Analysis*, page 103500, 2025.
- [50] Salman Ul Hassan Dar, Marvin Seyfarth, Isabelle Ayx, Theano Papavassiliu, Stefan O. Schoenberg, Robert Malte Siepmann, Fabian Christopher Laqua, Jannik Kahmann, Norbert Frey, Bettina Baeßler, Sebastian Foersch, Daniel Truhn, Jakob Nikolas Kather, and Sandy Engelhardt. Unconditional latent diffusion models memorize patient imaging data: Implications for openly sharing synthetic data. *Nature Biomedical Engineering*, 2024.
- [51] Marc Bazot, Annie Cortez, Emile Darai, Jérôme Rouger, Jocelyne Chopier, Jean-Marie Antoine, and Serge Uzan. Ultrasonography compared with magnetic resonance imaging for the diagnosis of adenomyosis: correlation with histopathology. *Human Reproduction*, 16(11):2427–2433, November 2001.
- [52] Sébastien Novellas, Madleen Chassang, Jerome Delotte, Olivier Toullalan, Anne Chevallier, Jerome Bouaziz, and Patrick Chevallier. Mri characteristics of the uterine junctional zone: From normal to the diagnosis of adenomyosis. *American Journal of Roentgenology*, 196(5):1206–1213, May 2011.
- [53] Anindo Saha, Joeran S Bosma, Jasper J Twilt, Bram van Ginneken, Anders Bjartell, Anwar R Padhani, David Bonekamp, Geert Villeirs, Georg Salomon, Gianluca Giannarini, et al. Artificial intelligence and radiologists in prostate cancer detection on mri (pi-cai): an international, paired, non-inferiority, confirmatory study. *The Lancet Oncology*, 25(7):879–887, July 2024.
- [54] Jordina Aviles Verdera, Sara Neves Silva, Kelly M. Payette, Raphael Tomi-Tricot, Megan Hall, Lisa Story, Shaihan J. Malik, Joseph V. Hajnal, Mary A. Rutherford, and Jana Hutter. Real-time fetal brain and placental t2* mapping at 0.55t mri. *Magnetic Resonance in Medicine*, 94(2):615–624, March 2025.

- [55] Jordina Aviles Verdera, Antonia Bortolazzi, Sara Neves Silva, Kelly Payette, Kamilah St. Clair, Sarah McElroy, Shaihan Malik, Joseph Hajnal, Raphael Tomi-Tricot, Mary Rutherford, and Jana Hutter. Heron: High-efficiency real-time motion quantification and re-acquisition for fetal diffusion mri. *IEEE Transactions on Medical Imaging*, page 1–1, 2025.
- [56] Megha M Anchan, Guruprasad Kalthur, Ratul Datta, Kabita Majumdar, Karthikeyan P, and Rahul Dutta. Unveiling the fibrotic puzzle of endometriosis: An overlooked concern calling for prompt action. *F1000Research*, 13:721, December 2024.